N-bridged Ni and Mn single-atom pair sites: A highly efficient electrocatalyst for CO_2 conversion to CO

Hyunsu Han [*], Juhwan Im, Myungsuk Lee, Daehyun Choo

Institute of Environmental Science & Technology, SK innovation Co., 325 Expo-ro, Yuseong-gu, Daejeon 34124, South Korea

ARTICLE INFO

ABSTRACT

Herein, we report highly efficient diatomic electrocatalysts with Ni and Mn single-atom pair sites decorated on N-doped porous carbon framework for CO_2 conversion. The resulting catalysts can preferentially and rapidly convert CO_2 into CO with a high Faradaic efficiency of 98.3% and an industrially relevant current density of -300 mA cm^{-2} at a low overpotential of 0.287 V in a GDE-based flow reactor cell. Furthermore, it shows high cathodic energetic efficiencies over 80 % for CO production even under industrially relevant current densities. The in-depth experimental measurements and theoretical calculations reveal that the synergistic electronic modification effect caused by coupling neighboring Ni and Mn single atoms exhibits favorable characteristics in reaction steps of CO_2 conversion such as CO_2 adsorption/activation and immobilization of CO_2 radical intermediate as well as adsorbed CO desorption, leading to highly efficient CO production.

1. Introduction

The tremendous use of fossil fuels for energy demand leads to the accumulation of greenhouse gases such as CO_2 in the atmosphere contributing to serious environmental issues [1,2]. As a remedy, conversion of CO_2 into value-added chemicals using electrolysis is one of the most proper approaches due to its various technological advantages over other strategies [3,4]. Nonetheless, the current electrochemical CO_2 reduction reaction (CO_2RR) process still has challenges of a high reaction barrier required for sufficient reaction rates, complexity of reaction products and unavoidable competitive hydrogen evolution reaction (HER), which should limit the practical CO_2 electrolysis [5,6]. In this sense, it is desirable to develop highly active and selective heterogeneous electrocatalysts for CO_2RR.

Single-atom catalysts (SACs) with extremely high atomic efficiency, unique geometric/electronic structure, and well-defined catalytic sites have shown appealing electrocatalytic CO_2RR performances for CO production [7–9]. However, the structural simplicity of single-atom sites in SACs fundamentally limits the efficiency of catalytic reaction due to the multistep-coupled proton-electron transfer of CO_2RR process. For example, Ni and Cu SACs generally show excellent catalytic properties for adsorbed CO (*CO) desorption and suppression of HER, but sluggish kinetics of the first electron-proton transfer step [10,11]. Meanwhile, Fe and Co SACs exhibit a low energy barrier to form adsorbed COOH

intermediate (*COOH), while suffer from the desorption of *CO due to the strong CO affinity [12,13]. To solve these issues, an intriguing strategy is to form hetero-diatomic structures (referred to as diatomic catalysts; DACs) with distinctive geometric and electronic nature by introducing additional metal atoms into SACs. Currently, a variety of diatomic catalysts (DACs) have emerged and have attracted much attention owing to their excellent electrocatalytic properties to selective CO_2-to-CO conversion compared with SACs [14–16]. The modified electronic structure of DACs induced by interaction between neighboring hetero-diatomic sites has a substantial impact on reactant/intermediate adsorption, energy barriers, and reaction kinetics, breaking the intrinsic limits and maximizing the potential of SACs for CO_2RR [17,18]. Very recently, Luo *et al.* theoretically investigated the CO_2RR performance of different DACs where five 3d metals (Ni, Cu, Co, Fe and Mn) were considered. Among DACs consisting of two different metal atoms, Ni-Fe, Cu-Mn and Ni-Mn DACs possessed a favorable *COOH adsorption strength and a moderate *CO adsorption strength, showing that these catalysts hold great potential to serve as promising candidates for selective CO production [19]. Although Ni-Mn DACs were demonstrated to be a highly efficient CO_2RR catalyst by theoretical calculations, to the best our knowledge, the experimental studies on development of DACs consisting of Ni-Mn hetero-diatomic pairs for electrocatalytic CO_2 conversion have been rarely reported. Meanwhile, previous work reported that the strong electronic interaction of adjacent

---

* Corresponding author.
E-mail address: han.hs@sk.com (H. Han).

Ni and Mn species in organic framework nanosheets could cause the changes in electronic structure of Ni active centers, tuning the adsorption energies of intermediates and subsequently resulting in the enhanced oxygen electrocatalysis activity [20]. In this regard, for the CO_2RR process, it is hypothesized that the modification of the electronic structure of Ni-Mn DACs induced by synergistic coupling between neighboring Ni and Mn atoms can give rise to the appropriate binding strength of the key intermediates, which may be favorable for highly efficient CO_2 electroreduction. However, it remains a great challenge to fabricate the DACs with superior CO_2RR performance via an effective synthetic method, which is of significance for technological advances in the field of CO_2RR to realize the industrial applications.

Herein, a novel electrocatalyst featuring N-bridged Ni-Mn diatomic sites supported on N-doped porous carbon framework (NiMn DAC) has been developed via a facile ion adsorption process and, for the first time, used to the cathodic catalysts in a GDE-based flow reactor cell for the CO_2RR. For electrocatalytic CO production, the NiMn DAC shows a high Faradaic efficiency of 98.3 % with an industrially relevant current density of – 300 mA cm^{-2} at low overpotential of 0.287 V, equivalent to high cathodic energetic efficiency over 80 %. Compared with Ni single-atom catalysts (Ni SAC), its superior performance can be mainly derived from the electronic tuning effect of Ni and Mn sites through the two shared N bridge, leading to the rapid charge transfer kinetics, enhanced adsorption strength of CO_2 and reaction intermediate as well as efficient *CO desorption. In this work, the effects of electronic interaction of N-bridged hetero-diatomic pairs are systemically elucidated to understand the remarkably improved CO_2RR performance.

2. Experimental section

2.1. Chemicals and reagents

Sodium citrate tribasic dihydrate ($C_6H_5Na_3O_7 \cdot 2H_2O$, Sigma Aldrich), pyrrole (C_4H_5N, Sigma Aldrich), ammonium persulfate (($NH_4)_2S_2O_8$, Sigma Aldrich), sulfuric acid (H_2SO_4, Sigma Aldrich), hydrochloric acid (HCl, Sigma Aldrich), potassium hydroxide (KOH, Sigma Aldrich), ethanol (C_2H_5OH, Sigma Aldrich), nickel nitrate hexahydrate (Ni $(NO_3)_2 \cdot 6H_2O$, Sigma Aldrich), manganese nitrate hexahydrate (Mn $(NO_3)_2 \cdot 6H_2O$, Alfa Aesar), nickel phthalocyanine ($C_{32}H_{16}N_8Ni$, Sigma Aldrich), manganese phthalocyanine ($C_{32}H_{16}N_8Mn$, Sigma Aldrich), Sigracet 39BB carbon paper (Dioxide Materials), commercial Ag/C electrode (Dioxide Materials) and deionized water (DI, Millipore) were used for the entire experiments in this work.

2.2. Synthesis of catalysts

The porous carbon (PC) was synthesized by direct pyrolysis of sodium citrate tribasic dihydrate at 800 °C for 1 h in an inert atmosphere. Then, the obtained powder was treated with 1 M H_2SO_4 solution for eliminating inorganic residues. After 2 h, the carbon product was washed several times with DI water and dried in an oven. For synthesis of Ni-Mn diatomic catalysts (NiMn DAC), 700 mg of porous carbon was firstly dispersed in 80 mL of ethanol/DI water mixtures (volume ratio 3:1) by using ultrasonication treatment for 0.5 h, followed by pyrrole monomer (2.2 mmol) addition. Then, ammonium persulfate (2.6 mmol) in DI water (10 mL) was added dropwise to the above suspension under stirring for 2 h to obtain the polypyrrole-coated porous carbon composite (PPyPC). Next, the decoration of Ni and Mn species on PPyPC were achieved via a facile ion adsorption process. Typically, 200 mg of PPyPC powder was added into 40 mL of metal nitrate stock solution (0.5 mg mL^{-1} of Ni^{2+} solution and 0.5 mg mL^{-1} of Mn^{2+} solution) under stirring overnight and collected to obtain the Ni^{2+}-Mn^{2+}-PPyPC powder. Finally, the resulting Ni^{2+}-Mn^{2+}-PPyPC was heat-treated at 800 °C for 1 h under an inert atmosphere and washed with 1 M HCl solution and denoted as NiMn DAC. For comparison, Ni single-atom catalyst (Ni SAC) and Mn single-atom catalyst (Mn SAC) were also prepared according to

the same procedure as that used to prepare the NiMn DAC but without employing Mn^{2+} solution and Ni^{2+} solution, respectively. Additionally, N-doped porous carbon (NPC) was synthesized through a similar procedure but without addition of metal nitrate stock solution.

2.3. Physicochemical characterizations

The surface morphologies of samples were investigated by scanning electron microscopy (SEM) images, as collected on a JSM-7401 F instrument. High-resolution transmission electron microscopy (HR-TEM), aberration-corrected high-angle annular dark-filed scanning transmission electron microscopy (HAADF-STEM) and electron energy-loss spectroscopy (EELS) line scan were conducted on a JEM-2200 FS instrument with image Cs-corrector. X-ray diffraction (XRD) patterns were obtained by an Empyrean (PANalytical) and Fourier transform infrared (FT-IR) spectrum was recorded by a Frontier (PerkinElmer) with KBr-sample pellet form. The actual metal concentrations of the samples were investigated by inductively coupled plasma-mass spectroscopy (ICP-MS, NexION 350S). The textural properties of samples such as specific surface area and pore volume were evaluated using N_2 adsorption/desorption isotherms by Quadrasorb SI instrument. Raman microscope was performed by using Renishaw (inVia) instrument. CO_2 uptake capability was investigated by a BELSORP-mini (MicrotracBEL) instrument. CO_2 temperature-programmed desorption (CO_2-TPD) measurements were conducted by injection of CO_2 gas for 1 h at 30 °C and the desorption of CO_2 was analyzed using TCD detector with increasing temperature from 30° to 300 °C at a heating rate of 5 °C min^{-1}. Prior to the CO_2-TPD measurements, the pre-treatment of samples was performed at 300 °C with He atmosphere for 1 h. High-performance X-ray photoelectron spectroscopy (HP-XPS) spectra were collected on a VG multilab 2000 to determine the compositions and the oxidation states of catalysts. The X-ray absorption fine structure (XAFS) spectra (Ni K-edge and Mn K-edge) were recorded at the Pohang Accelerator Laboratory (PAL; PLS-II, 8C beamline).

2.4. Electrochemical measurements

All electrochemical tests were conducted in a home-made gas diffusion electrode (GDE)-based flow reactor cell consisting of two compartments (anode and cathode), which were separated by a Sustainion anion exchange membrane (Dioxide Materials). A carbon paper (Dioxide Materials, 0.95 cm^2) was used as the cathode and the loading of catalyst was 1 mg cm^{-2}. NiFeMo composite and Hg/HgO (MMO) electrode were applied as the anode and the reference electrode, respectively. Linear sweep voltammetry (LSV) was performed in N_2- or CO_2-saturated 1 M KOH electrolyte at a scan rate of 20 mV s^{-1}. Chronopotentiometry measurements were conducted to estimate the CO_2 reduction products at – 40, – 70, – 120, – 200, – 300, – 350 and – 370 mA cm^{-2} and the corresponding applied potential was converted to a RHE with *iR*-drop compensation. During the chronopotentiometry measurements, 1 M KOH electrolyte was circulated between the cathode and the membrane with a flow rate of 1.5 mL min^{-1}. CO_2 gas was continuously fed into the cathodic compartment at a rate of 30 sccm. The CO and H_2 products were analyzed by using a gas chromatograph (GC, Agilent 7890). We also estimate the values of turnover frequency (TOF) for CO_2-to-CO conversion according to the following equation [14]:

$$TOF(h-1) = \frac{j_{CO}/nF}{m_{catal} \times \omega/M_{metal}} \times t$$

Where j_{CO} is the partial current density for CO generation, n is the number of electrons (CO_2-to-CO conversion; n:2), F is the Faraday constant (96,485 C mol^{-1}), t is 3600, m_{catal} is the mass of catalyst coated on the cathode (g cm^{-2}), ω is the metal species content (wt% based on ICP data), and M_{metal} is the atomic mass of metal based on the ratio of Ni and Mn (NiMn DAC: 57.19 g mol^{-1}, Ni SAC: 58.69 g mol^{-1} and Mn SAC:

54.94 g mol^{-1}). Tafel slope was determined from the equation (η = blog (j_{CO}/j_o)), where b is the Tafel slope, j_{CO} is partial current density for CO production, j_o is exchange current density and η is overpotential. Nyquist plots were recorded from 10 kHz to 10 MHz at an AC voltage of 10 mV. Cyclic voltammogram (CV) measurements were carried out to obtain the capacitive currents at various scan rates (5, 10, 20 and 40 mV s^{-1}) in the applied potential range from 0.56 to 0.80 V (vs RHE). The cathodic energetic efficiency (EE) for CO production was estimated according to the following equation:

$$\text{Cathodic EE}(\%) = \frac{1.23\text{V} - \text{E}_{CO}}{1.23\text{V} - \text{E}_{\text{Cathode}}} \times \text{FE}_{CO}$$

Where 1.23 V (vs RHE) is the thermodynamic potential for water oxidation on the anode side, E_{CO} is the thermodynamic potential for CO production from CO$_2$ conversion (– 0.11 V vs RHE) and E_{Cathode} is the applied cathodic potential (V vs RHE).

2.5. Computational details

Density functional theory (DFT) calculations were conducted using the Vienna ab initio simulation package (VASP) [21–23] with the generalized gradient approximation (GGA) of the Perdew-Burke-Ernzerhof (PBE) to treat the exchange functional [24], and the core electrons were demonstrated with the projection augmented wave (PAW) method [25] under the Born-Oppenheimer
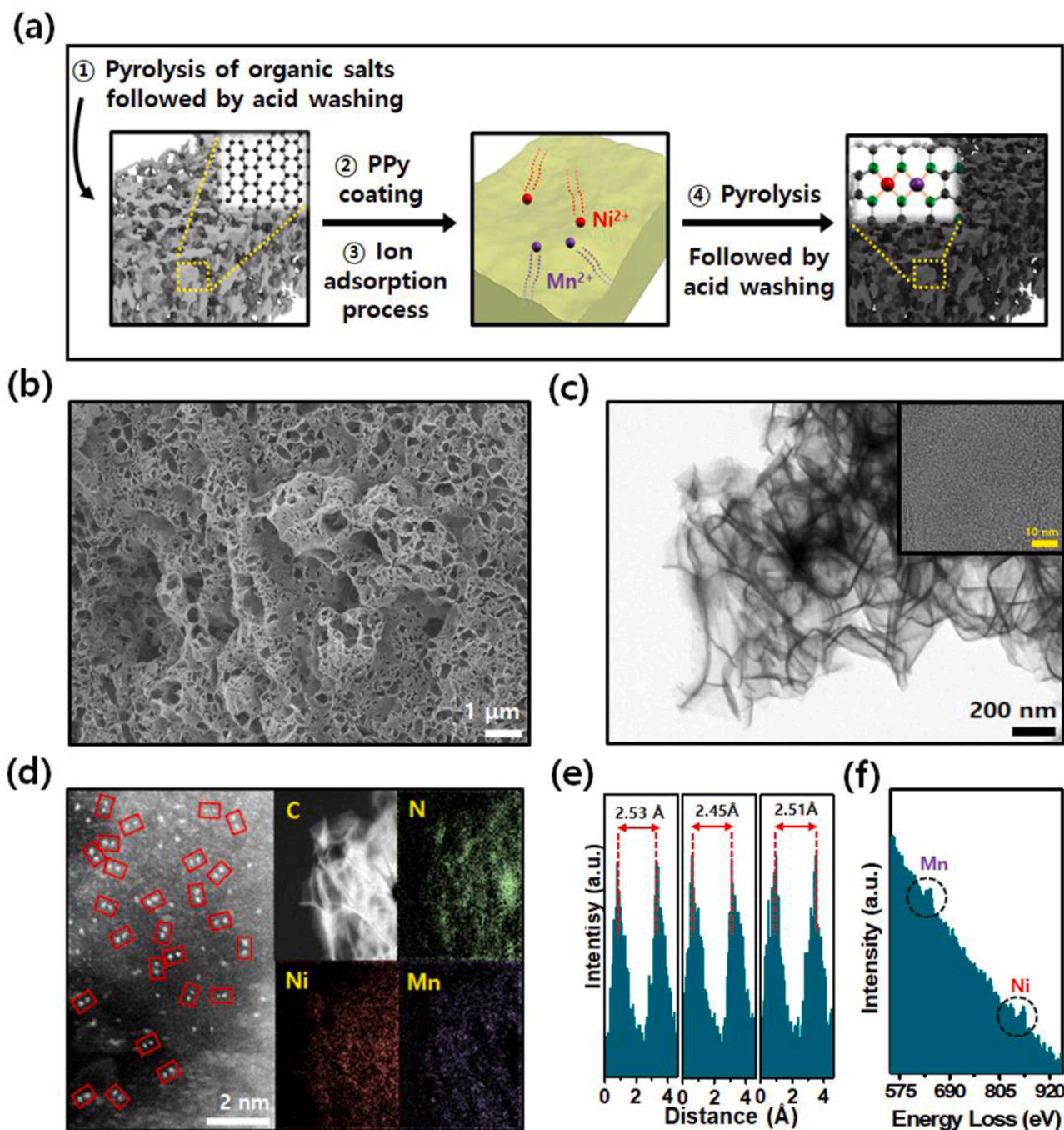
Fig. 1. (a) Schematic illustration of the overall synthesis process for NiMn DAC. (b) SEM image, (c) TEM image; inset shows the HR-TEM image, (d) HAADF-STEM image with elemental mappings, (e) intensity profiles and (f) EELS spectrum of NiMn DAC extracted from Fig. 1d.

approximation. The DFT+D2 method was included to consider the van der Waals interactions [26]. A cubic graphene layer (12.82×12.34 Å^2) with vacuum (20 Å) was used to avoid periodical interactions of the system. In structural optimization, a ($1 \times 1 \times 1$) mesh of k points in the Monkhorst-Pack [27] and 400 eV cutoff energy was selected. For geometry relaxation, the convergence standards of total energy and residual atomic forces were adapted as 10^{-5} eV and 0.05 eV Å^{-1}.

3. Results and discussion

3.1. Characterizations of catalysts

Fig. 1a indicates schematic of the overall synthesis procedures for NiMn DAC. Briefly, the porous carbon materials were firstly synthesized by facile carbonization process using sodium citrate as carbon framework source, and then polypyrrole as N source was coated on porous carbon via in situ polymerization. Finally, the facile ion adsorption process was employed with nickel and manganese nitrate stock solution, followed by filtration and heat treatment under an inert atmosphere. Owing to the presence of N functional group with lone pair of electrons
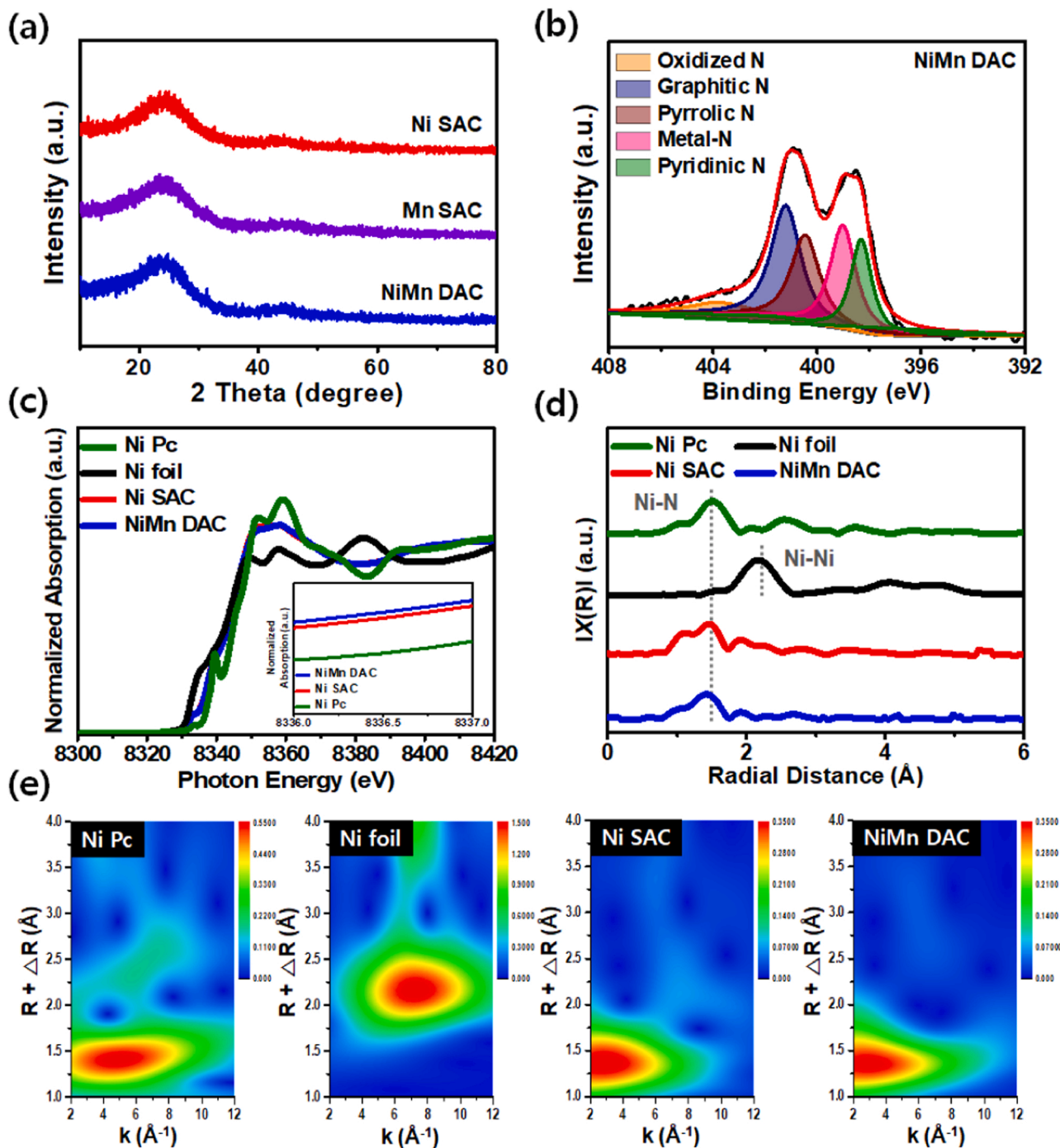

Fig. 2. Structural characterizations. (a) XRD patterns, (b) high-resolution N 1s XPS spectra, (c) Ni K-edge XANES spectra; inset shows the comparison in detail, (d) k^2-weighted Ni K-edge FT-EXAFS spectra and (e) Ni K-edge WT-EXAFS contour plots.

in polypyrrole backbone [28], polypyrrole-coated porous carbon composite can possess a high adsorption capacity to Ni and Mn cation in aqueous solution. Initially, the FT-IR spectrum was investigated to confirm the successful coating of polypyrrole onto porous carbon material (PPyPC). Fig. S1 represents two peaks at 1558 and 1473 cm^{-1} for the stretching vibrations of C-C and C-N bonds, respectively, and the peak at 1045 cm^{-1} can be assigned to C-H in-plane vibration in the pyrrole ring. These characteristic peaks suggest the successful fabrication of polypyrrole-coated porous carbon composite [29]. As displayed by scanning electron microscopy (SEM) and transmission electron microscopy (TEM) images (Fig. 1b,c), the NiMn DAC shows a well-developed porous framework with numerous open pores in multidirectional channels. In addition, high-resolution TEM (HR-TEM) image shows disordered and amorphous carbon structures with no aggregation of metallic nanoparticles (the inset of Fig. 1c). The atomically dispersed Ni and Mn species were verified by aberration-corrected high-angle annular dark-field scanning transmission electron microscopy (HAADF-STEM). Fig. 1d clearly reveals the existence of diatomic sites and the corresponding elemental mappings also indicate the uniform distribution of Ni, Mn, and N species over the entire porous carbon. As displayed in Fig. S2a, statistical analysis of atoms in NiMn DAC confirm that most of the atoms exist in the form of two adjacent atoms with the ratio of 68 %, followed by 32 % of isolated single atoms. Meanwhile, most of neighboring atoms are noticed with a typically average distance of ~ 2.55 Å, implying the possible formation of single-atom pairs in NiMn DAC (Fig. 1e and Fig. S2b). Additionally, the electron energy-loss spectroscopy (EELS) spectrum extracted from Fig. 1d clearly represents the coexistence of Ni and Mn species in NiMn DAC (Fig. 1f). For comparison, the surface morphologies of Ni SAC and Mn SAC are presented in Figs. S3 and S4, which were synthesized by a similar method as that of NiMn DAC.

The crystal structures of the prepared catalysts were obtained by X-ray diffraction (XRD) and Raman spectroscopy. As depicted in Fig. 2a, all catalysts present one broad diffraction peak at around 24°, which are assigned to the (002) crystal face of carbon with low crystallization [30]. Notably, there are no remarkable peaks related to crystalline Ni and Mn species, indicating a high dispersion of Ni and Mn species throughout the surface of N-doped porous carbons without nanoparticle formation. From the Raman spectra of Fig. S5, two strong peaks located at 1335 cm^{-1} (D band) and 1580 cm^{-1} (G band) are observed, which are associated with disordered carbon and graphitic sp^2-hybridized carbon, respectively [31]. The relative intensities of the D and G bands are close to each other (I_D/I_G: ~ 0.45), suggesting a similar graphitization degree of the porous carbons. The textural properties were further analyzed by N$_2$ sorption measurement (Fig. S6 and Table S1). The isotherm curves show that all catalysts possess similar textural properties with Brunauer-Emmett-Teller (BET) surface area and porosity feature. Obviously, such a porous structure with large BET surface area is favorable to exposing more accessible catalytic sites and accelerating transportation of electrons and CO$_2$RR-related species [31–33].

High-performance X-ray photoelectron spectroscopy (HP-XPS) was carried out to investigate the surface compositions and the electronic states of prepared catalysts. As shown in Fig. 2b, Fig. S7a-c and Table S2, high-resolution N 1s spectra display four peaks at around 398.3, 400.5, 401.2 and 403.5 eV, which are ascribed to the binding energies of pyridinic N, pyrrolic N, graphitic N and oxidized N, respectively. Notably, the porphyrin-like portions centered at around 399.1 eV of Ni SAC, Mn SAC and NiMn DAC can be associated with metal-N coordination, implying that the Ni and Mn atoms are bonding with N species on the porous carbon [34–36]. In addition, as previously reported [37,38], pyridinic N species in N-doped carbon play an essential role in anchoring and stabilizing isolated transition metal atoms. After the incorporation of Ni and Mn species, the content of pyridinic N is significantly decreased whereas there is no noticeable change in the contents of pyrrolic N, graphitic N and oxidized N (Fig. S7d). The significant decrease in the relative content of pyridinic N suggested that most of Ni

and Mn atoms favorably coordinate with pyridinic N. The concentrations of metal-N species are 19.5 %, 15.8 % and 22.6 % in total N species for Ni SAC, Mn SAC and NiMn DAC, respectively, matching well with the observation that NiMn DAC has a higher concentration of metal species revealed by inductively coupled plasma atomic emission spectroscopy (ICP-AES) (Table S3). In the high resolution of Ni 2p spectra (Fig. S8a), the binding energies of Ni 2p$_{3/2}$ in NiMn DAC and Ni SAC are lower than that of nickel phthalocyanine (NiPc; Ni^{2+}). Also, the Mn 2p$_{3/2}$ peaks of NiMn DAC and Mn SAC shift to lower binding energies compared to Mn phthalocyanine (MnPc) (Fig. S8b). These XPS results suggest that the Ni and Mn species in prepared catalysts are likely to be in a partially oxidized state. Notably, the negative shift (0.4 eV) of the binding energy of Ni 2p$_{3/2}$ and the positive shift (0.5 eV) of the binding energy of Mn 2p$_{3/2}$ in NiMn DAC indicate an electronic tuning effect of neighboring Ni and Mn atoms [39].

To further explore the detailed atomic structure and chemical environments of prepared catalysts, synchrotron-based X-ray absorption near-edge structure (XANES) and extended X-ray absorption fine structure (EXAFS) were investigated. As depicted in Ni K-edge XANES spectra (Fig. 2c), the near-edge absorption energies of NiMn DAC and Ni SAC are positioned between those of Ni(0) foil and Ni(II) phthalocyanine (NiPc), further indicating partially positive charges with a oxidation state between 0 and + 2. In comparison with Ni SAC, the negative shift of near-edge features of NiMn DAC manifests a decreased oxidation state of Ni after the introduction of Mn atoms. Regarding the Ni K-edge spectra, an increased oxidation state of Mn is observed in NiMn DAC relative to Mn SAC (Fig. S9a). These results clearly reveal the electronic interaction involving charge transfer from Mn to Ni in N-bridged diatomic structure of NiMn DAC, which is in line with the XPS results. From the Ni K-edge Fourier-transformed (FT) k^2-weighted EXAFS spectra (Fig. 2d), the predominant peaks at around 1.5 Å for NiMn DAC and Ni SAC can be associated with Ni-N coordination. Regarding the Mn K-edge FT-EXAFS spectra (Fig. S9b), NiMn DAC and Mn SAC exhibit main peaks around 1.6 Å originating from Mn-N bond. However, no peaks of metal-metal bonds including Ni-Ni (2.2 Å) and Mn-Mn (2.4 Å) are observed, suggesting the atomic dispersion of both Ni and Mn species on N-doped porous carbons [10,35]. In addition, wavelet transform (WT) of EXAFS analysis for NiMn DAC and Ni SAC shows only one maximum intensity related with the Ni-N contributions and demonstrates that the majority of Ni species exist at the atomic level (Fig. 2e). A similar conclusion can also be deduced from the Mn K-edge WT-EXAFS as shown in Fig. S9c. The average Metal-N coordination number obtained from Ni and Mn K-edge EXAFS fittings further demonstrates that atomic Ni and Mn centers in NiMn DAC, Ni SAC and Mn SAC mainly coordinated with four N atoms, suggesting Ni-N$_4$ and Mn-N$_4$ configurations (Fig. S10, Table S4 and Table S5). To determine the specific structure of NiMn DAC, different structure models have been proposed by using software Materials Studio. From structural simulations (Fig. S11), model A has the most consistent interatomic distance (~ 2.5 Å) and coordination environment with the experimental results of HAADF-STEM and XAFS measurements, demonstrating the most optimized structure in NiMn DAC. Consequently, NiMn DAC contains both Ni-N$_4$ and Mn-N$_4$ moieties, and neighboring Ni and Mn atoms interact indirectly through two shared N bridge (model A), which might act as the intrinsic driving force to form Ni-Mn single-atom pairs.

3.2. CO$_2$RR performance of catalysts

Electrochemical experiments of all catalysts were conducted in a home-made GDE-based flow reactor cell consisting of two compartments (cathode/anode) which were separated by anion exchange membrane. The CO$_2$RR activity of prepared catalysts was initially investigated by linear sweep voltammetry (LSV) in an inert atmosphere saturated- or CO$_2$-saturated 1 M KOH electrolyte (Fig. 3a). The cathodic current densities of all catalysts observed in N$_2$-saturated electrolyte are entirely attributed to the HER. Notably, NiMn DAC indicates a larger current
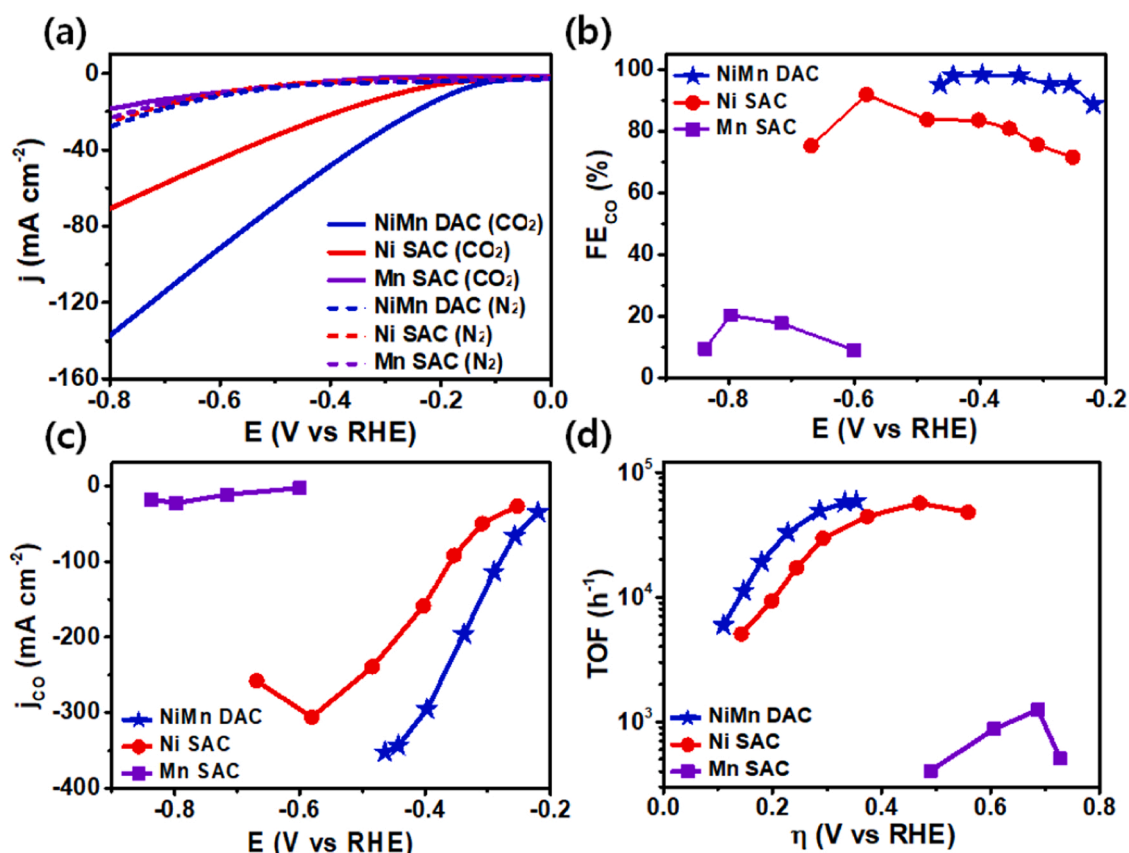
Fig. 3. CO$_2$RR performance. (a) LSV curves, (b) FE for CO production analyzed by chronopotentiometry and (c) corresponding partial current density and (d) TOF values of Ni SAC, Mn SAC and NiMn DAC; Electrochemical measurements were performed in GDE-based flow reactor cell.

density in CO$_2$-saturated electrolyte than in N$_2$-saturated electrolyte. The comparison of polarization curves demonstrates that NiMn DAC is more active toward CO$_2$ conversion than to H$_2$ production. Furthermore, a more positive onset potential with a larger current density of NiMn DAC in the presence of CO$_2$ than that of Ni SAC and Mn SAC is observed, suggesting the best catalytic activity for CO$_2$RR. Chronopotentiometry measurements were conducted to assess the CO$_2$RR products and the Faradaic efficiency profiles for CO production (FE$_{CO}$) of the prepared catalysts displayed in Fig. 3b. Among them, NiMn DAC exhibits the highest FE$_{CO}$ of 98.3 % at − 0.397 V (vs RHE) and over 95 % from − 0.257 to − 0.464 V (vs RHE), outperforming the other two counterparts across the entire potential region. Additionally, the FE$_{CO}$ of Ni SAC reached a maximum value (91.9%) at more negative potential of − 0.580 V (vs RHE) and rapidly decreased to lower values subsequently. This result agrees with the previous studies, where Ni single-atom sites displayed kinetically sluggish of the formation of *COOH intermediate [10,11]. Meanwhile, Mn SAC shows the lowest FE$_{CO}$, which is due to lack of catalytic ability of Mn single-atom sites toward CO$_2$ reduction [40]. Notably, NiMn DAC shows the lowest FE for H$_2$ generation, indicating the excellent capability for suppression of hydrogen evolution reaction (HER) (Fig. S12). There were no other products and total FE for CO and H$_2$ production equaled to about 100%. Also, the partial current densities for CO production (j$_{CO}$) of the prepared catalysts were investigated as presented in Fig. 3c. Remarkably, NiMn DAC exhibits a higher catalytic performance than Ni SAC and Mn SAC in all measured potential region. For example, NiMn DAC indicates much higher j$_{CO}$ (− 295 mA cm^{-2} at − 0.397 V vs RHE) than Ni (− 159 mA cm^{-2} at − 0.403 V vs RHE), highlighting great superiority of Ni-Mn DAC. Moreover, electrochemical active surface area (ECSA) and BET surface area of NiMn DAC are similar to Ni SAC and Mn SAC (Fig. S13 and Table S1), further demonstrating that excellent CO$_2$RR performance originates from better intrinsic

activity of neighboring Ni-Mn single-atom pairs in NiMn DAC. It is worth noting that the industrial-level current density (> 200 mA cm^{-2}) is one of the most important target performance metrics for realizing the commercialization of CO$_2$RR [41,42]. Notably, NiMn DAC achieves an industrially relevant current density (> − 300 mA cm^{-2}) for CO production with over 95 % FE in overpotential range from − 0.287 to − 0.354 V (vs RHE), demonstrating practically meaningful CO$_2$RR performance. From Table S6, newly developed NiMn DAC is one of the best catalysts for CO$_2$RR to CO production in comparison with state-of-the-art single-atom and diatomic catalysts reported previously. Long-term durability is another important requisite for the development of an ideal CO$_2$RR catalyst. The durability test was carried out at constant current density of − 100 mA cm^{-2} and a fresh 1.0 M KOH electrolyte was continuously supplied to the cathode compartment. As revealed in Fig. S14, NiMn DAC shows negligible activity degradation and the corresponding FE$_{CO}$ retains a high value (> 95 %) during CO$_2$RR, highlighting the excellent durability. This result suggests that the strong interaction between Ni, Mn and N-doped sites in NiMn DAC might effectively maintain the catalytic properties of active sites, which could extend the life of catalysts.

More importantly, the operating cost of electrocatalytic system is significantly influenced by the consumption of electricity, which can be determined by the energetic efficiency (EE) of the electrochemical system. Therefore, achieving high energetic efficiency at industrially relevant current density is essential to make CO$_2$RR economically viable. Although high FE$_{CO}$ has been previously reported, the accomplishment of high EE is restricted by large cathodic overpotential at high current density of hundreds of mA cm^{-2} [43–45]. In our work, owing to the high FE$_{CO}$ and low overpotential, NiMn DAC attains a high cathodic EE of 83.9%, 83.8% and 81.0% for total current densities of − 120, − 200 and − 300 mA cm^{-2}, respectively, which are comparable and much higher

than the best previous reports using KOH electrolyte (Fig. S15 and Table S7). Also, it is notable that the CO_2RR performance for newly developed NiMn DAC outperforms the commercial Ag/C catalyst (Fig. S16). To rule out the effect of metal concentrations on j_{CO}, we further evaluate the turnover frequency (TOF) to confirm the intrinsic activity of prepared catalysts (Fig. 3d). Specifically, NiMn DAC shows a high TOF value of 49,255 h^{-1} at overpotential of 0.287 V (vs RHE), which is much higher than those of Ni SAC (29,488 h^{-1} at 0.293 V) and Mn SAC (403 h^{-1} at 0.491 V), respectively, manifesting an intrinsically higher CO_2RR activity of NiMn DAC. These results indicate that NiMn DAC shows outstanding catalytic performance toward the highly selective CO_2-to-CO conversion, which may be ascribed to the significant synergy between neighboring Ni and Mn single-atom pairs. This will be discussed in the following sections on the basis of detailed experimental characterizations.

To obtain further insights into the improved CO_2RR performance on NiMn DAC, we analyzed the Tafel slopes, Nyquist plots, single oxidative LSV curves, CO_2 capture capacity and CO_2 temperature-programmed desorption (CO_2-TPD). As the morphology, textural properties, graphitization degree and total N concentrations were not much different in Ni SAC, Mn SAC and NiMn DAC, the effect of Ni-Mn pair sites on CO_2RR performance can be independently elucidated. Fig. 4a displays the Tafel slopes obtained from the plotted logarithm of overpotential versus partial current density for CO production in which a lower magnitude of the Tafel slope indicates faster reaction kinetics for CO_2RR [46,47]. The Tafel slope of NiMn DAC is 154 mV dec^{-1}, which is much lower than that of Ni SAC (192 mV dec^{-1}) and Mn SAC (230 mV dec^{-1}), demonstrating that electrochemical CO_2-to-CO conversion is kinetically more favorable over the NiMn DAC compared to the others. Such a rapid reaction kinetic of NiMn DAC were also proved by electrochemical impedance spectroscopy (EIS) measurements. From Nyquist plots of

Fig. 4b, the smaller semicircle radius suggests the improved interfacial electron transfer ability of NiMn DAC, which is related to the lower activation energy barrier for CO_2RR process by the formation of stable adsorption of C=O configuration [48,49]. Additionally, it has been reported that the first step of CO_2RR is the initial production of CO_2 radical anion intermediate ($CO_2^{\bullet-}$) by one electron-transfer reaction at the surface of electrode during CO_2 activation process [31,50]. However, the accurate investigation of quantitative information and direct electrochemical behavior of $CO_2^{\bullet-}$ species still remain challenges because it is extremely unstable in the electrolyte and subsequently can form thermodynamically more stable intermediates through multiple proton-coupled electron-transfer steps. However, in CO_2RR process, the free electron of $CO_2^{\bullet-}$ species will be donated to the unoccupied orbital of catalyst, adsorbed $CO_2^{\bullet-}$ is chemically equivalent to adsorbed CO_2^- anion species (i.e., $*CO_2^-$) [50]. In this sense, the adsorption of OH^- anion species was employed as a surrogate to investigate the binding energy of $CO_2^{\bullet-}$ species on the surface of catalysts by single oxidative LSV experiments (Fig. 4c) [31,51]. The peak position for OH^- adsorption of NiMn DAC is more negative than that of Ni SAC and Mn SAC, indicating that NiMn DAC possessed a stronger binding strength for OH^-, and thus it could efficiently immobilize and stabilize CO_2 radical intermediate. Besides, the capability of CO_2 capture can substantially influence the catalytic activity and selectivity of catalysts for the CO_2RR [52,53]. As shown in CO_2 uptake of the prepared catalysts (Fig. 4d), the CO_2 adsorption capacity of NiMn DAC (2.48 mmol g^{-1}) is much larger than those of Ni SAC (1.76 mmol g^{-1}) and Mn SAC (0.42 mmol g^{-1}). Moreover, from CO_2-TPD measurements (Fig. S17), the shift of CO_2 desorption peak toward higher temperature means that CO_2 adsorption strength on NiMn DAC is stronger than that on Ni SAC and Mn SAC. Given the results of above measurements, the regulated electronic structure of NiMn DAC induced by interaction between neighboring
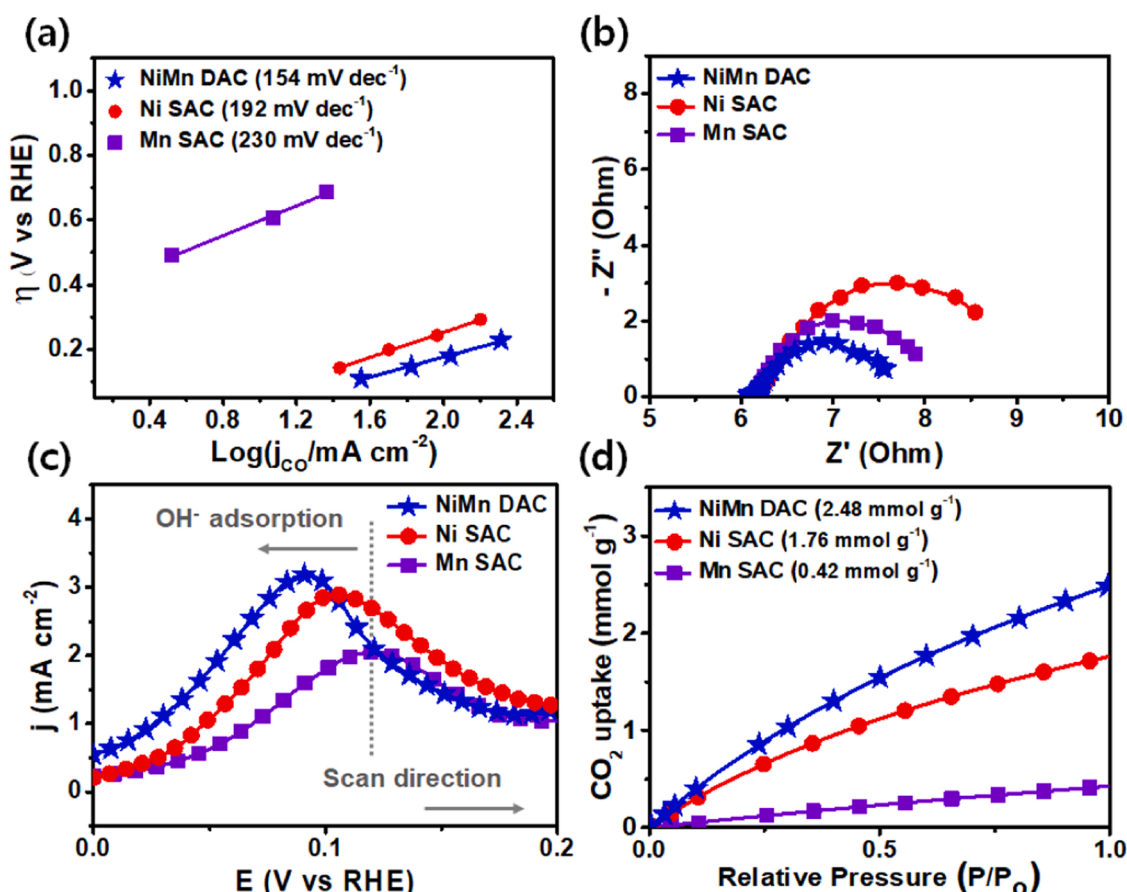

Fig. 4. (a) Tafel plots, (b) Nyquist plots, (c) Single oxidative LSV curves in 0.1 M KOH electrolyte and (d) CO_2 uptake at 25 °C of Ni SAC, Mn SAC and NiMn DAC.

Ni-N$_4$ and Mn-N$_4$ moieties evidently lead to the accelerated charge transfer and improved binding affinity of CO$_2$ and reaction intermediates.

3.3. Theoretical calculations for revealing the mechanism of the improved CO$_2$RR

We performed the density functional theory (DFT) calculations to clearly understand the influence of Mn-modification on the progress of CO$_2$RR over diatomic catalyst. In the presence of H$_2$O, the HER from reduction of H$_2$O is considered as a competitive cathodic reaction to the CO$_2$RR due to their similar thermodynamic potentials. In this regard, we first calculated the adsorption energies of H$_2$O as an initial reactant on different Ni and Mn sites of NiMn DAC. As shown in Fig. S18, the adsorption of H$_2$O is much more favored on Mn site in NiMn DAC (–0.31 eV) to further form the HER intermediates (competitive water reduction) in comparison with Ni site in NiMn DAC (– 0.12 eV), suggesting that H$_2$O could be readily adsorbed on Mn site and inhibit the adsorption of CO$_2$ in aqueous electrolyte. Then, we shifted our concern to inspect the CO$_2$RR activity of Ni site in NiMn DAC. Herein, the adsorbed *COOH and *CO are considered as the intermediates for CO production [54]. As observed in the reaction free energy profiles (Fig. 5a and Table S8), the difference of the free energy for *COOH formation on Ni site in NiMn DAC (0.71 eV) exhibits a lower activation energy barrier than Ni SAC (2.86 eV), representing that the *COOH is preferentially

adsorbed to the Ni site of NiMn DAC. Moreover, the *CO is more easily desorbed from the surface of NiMn DAC in comparison with Ni SAC, which is verified by the decreased free energy profile (0.13 eV vs 0.37 eV). These results unambiguously prove that CO$_2$RR performance of Ni site is remarkably improved by neighboring Mn-N$_4$ sites. Meanwhile, Mn SAC converts CO$_2$ with quite large exothermic energy to *CO and exhibits significantly high energy barrier of 2.43 eV for CO desorption. The strong *CO affinity of Mn SAC could lead to the CO$_2$RR performance loss due to poisoning effect [14,31], demonstrating why selective CO production is difficult on Mn SAC. As the HER is a competitive reaction upon CO$_2$RR, the free energy changes for HER are further examined (Fig. 5b and Table S9). The Ni site in NiMn DAC (1.52 eV) exhibits much higher energy barrier than Ni SAC (0.98 eV) for hydrogen adsorption, indicating an excellent HER suppression ability. From the results of reaction free energy profiles, the decreased free energy of *COOH adsorption and CO(g) formation as well as increased free energy of *H adsorption show the structural superiority of NiMn DAC toward CO$_2$RR, which is in line with the experimental observations. It is concluded that the introduction of the neighboring Mn-N$_4$ sites of NiMn DAC could regulate the adsorption/desorption energy of adsorbates on Ni site for highly efficient CO$_2$RR to selective CO production. We further conducted ultraviolet photoelectron spectroscopy (UPS) to examine the electronic state of NiMn DAC. As shown in the second electron cutoff edge region (Fig. S19a), the upward shift of binding energy for NiMn DAC compared with Ni SAC demonstrates a decrease in
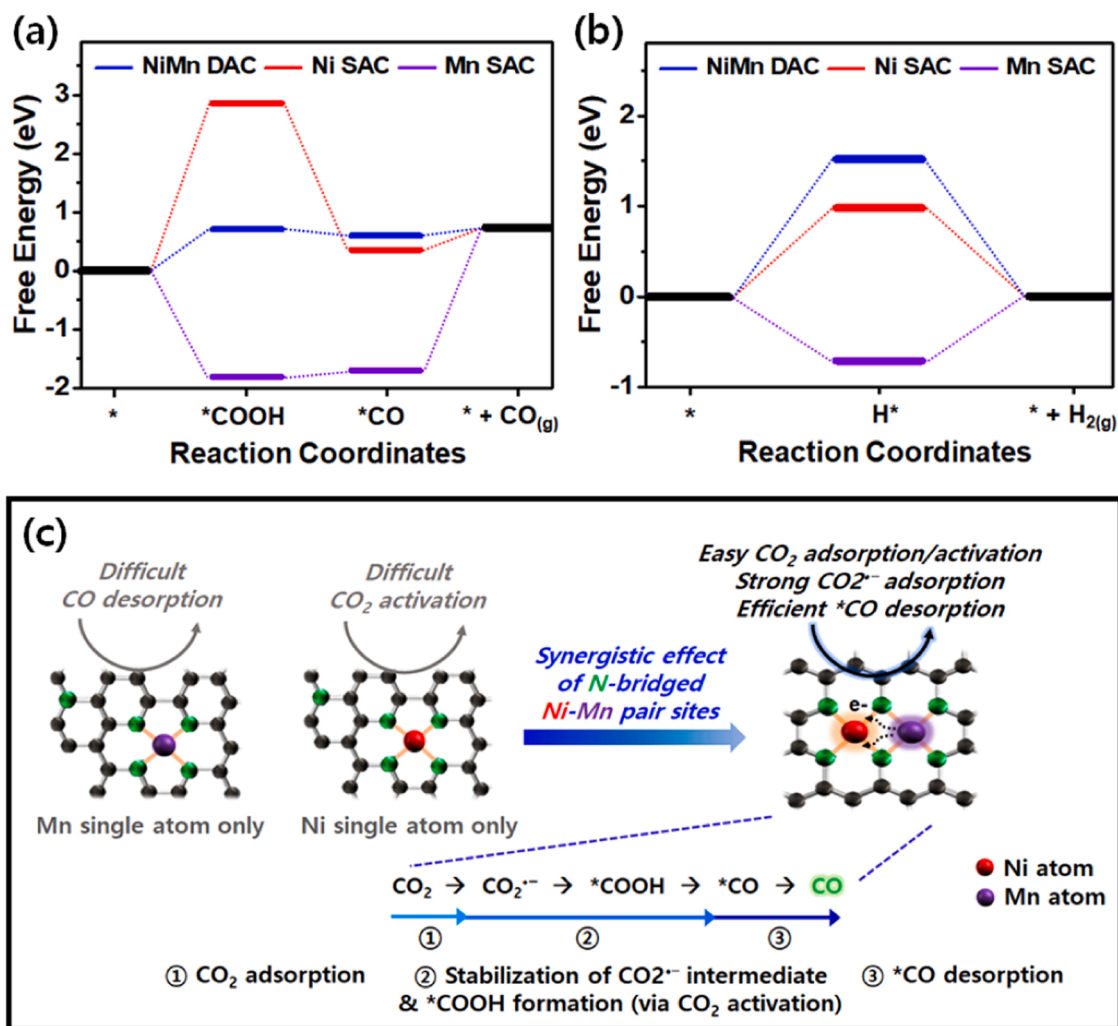

Fig. 5. DFT calculations. Free energy diagrams for (a) CO$_2$RR to CO production and (b) HER on Ni SAC, Mn SAC and Ni site in NiMn DAC. (c) Schematic illustration of highly efficient CO production on NiMn DAC.

work function which can accelerate the charge transfer to form *COOH intermediate from CO_2 [55]. In addition, NiMn DAC shows a higher electron density state than Ni SAC in the region of 0–4 eV (Fig. S19b). This is well matched with the DOS results, in which show that the total density of state (TDOS) of NiMn DAC has a larger electron density near the Fermi level as compared to that of Ni SAC (Fig. S20a). Also, it is noted that the projected density of states (PDOS) of Ni d orbitals in NiMn DAC displays a new peak close to the Fermi level, which is attributed by the introduction of secondary Mn atoms, suggesting a high electron density and mobility (Fig. S20b). Since the electrons at the Fermi level are the most active during chemical reactions, more electrons near the Fermi level can lead to reinforce the interaction between catalyst and CO_2RR-related species [52,56]. As revealed by the Bader charge analysis and differential charge density map (Table S10 and Fig. S21), the Bader charge of Ni site in NiMn DAC is decreased compared to that of Ni SAC, suggesting more charge accumulation at Ni site in the presence of neighboring Mn-N_4 moiety, which coincides with the XPS and XANES results. The unique electronic interaction between Ni and Mn atoms results in the lower oxidation state of Ni center in NiMn DAC, facilitating CO_2 adsorption and lowering the energy barrier of *COOH formation [57], as supported by Fig. 4a-d and Fig. S17. In this sense, a new strategy of DAC design developed in our work may offer a promising way to redeem the weak points and maximize performance of SAC for CO_2RR.

It is recognized that the electronic interaction between neighboring metal-metal single-atom pairs via shared N bridge can play vital roles in regulating the electronic property of active site, which may impart the DACs with excellent catalytic CO_2RR performance. Specifically, as demonstrated by recent work, in diatomic catalysts, the electronic structure of Fe atom can be modified by another adjacent Ni atom with Ni-N_4 moiety, which synergistically facilitate CO_2 adsorption and reduce the energy barrier for the formation of *COOH intermediate, leading to the improved CO_2RR performance [58]. Likewise, our findings clearly demonstrate that in NiMn DAC, the electronic tuning effect induced by coupling neighboring Ni and Mn atoms via two shared N bridge could lead to remarkably improved activity and selectivity toward CO production compared to Ni SAC and Mn SAC. Specifically, considering the results of experimental measurements and theoretical calculations presented herein and the previous studies comprehensively, it can conclude that Mn-modification effectively modulated the electronic structure of neighboring Ni atom with lower oxidation state through the electronic tuning effect, exhibiting favorable characteristics in CO_2RR steps such as CO_2 adsorption, $CO_2^{\cdot-}$ intermediate stabilization, CO_2 activation (*COOH formation) as well as *CO desorption, and these reaction steps are illustrated in Fig. 5c. Consequently, the modified adsorption properties of NiMn DAC result in highly efficient CO_2RR performance for selective CO production. Additionally, the strong interaction between Ni, Mn atoms and N-doped sites effectively retained the synergistic catalytic performance during electrolysis.

4. Conclusions

Herein, the atomically dispersed Ni and Mn species on N-doped porous carbon frameworks have been successfully synthesized as highly efficient diatomic catalysts for CO_2RR. Through neighboring Ni-Mn pair sites connected by two shared N species, the resulting NiMn DAC shows superior CO_2RR performance with a high Faradaic efficiency of 98.3% and an industrially relevant current density of – 300 mA cm^{-2} at a low overpotential of 0.287 V. Owing to the high FE_{CO} and low overpotential, it also exhibits a high cathodic energetic efficiency over 80% for CO production at – 300 mA cm^{-2}. The detailed experimental measurements and theoretical calculations demonstrate that the superior CO_2RR performance of NiMn DAC can be attributed to the synergistic electronic modulation effect of isolated Ni and Mn atoms in neighboring Ni-N_4 and Mn-N_4 moieties, leading to favorable characteristics in CO_2RR key steps and significantly accelerating the selective CO production accordingly. This work should give a new guideline for the rational design of DACs

and manifest the crucial importance of the synergistic effect between neighboring single atoms toward enhanced electrocatalysis.

CRediT authorship contribution statement

Hyunsu Han: Conceptualization, Methodology, Validation, Supervision, Data curation, Investigation, Writing – original draft, Writing – review & editing. **Juhwan Im:** Validation, Investigation, Data curation, Software. **Myungsuk Lee:** Validation, Data curation, Investigation, Software. **Daehyun Choo:** Validation, Project administration, Writing – review & editing.

Declaration of Competing Interest

The authors declare that they have no known competing financial interests or personal relationships that could have appeared to influence the work reported in this paper.

Data availability

Data will be made available on request.

Appendix A. Supporting information

Supplementary data associated with this article can be found in the online version at doi:10.1016/j.apcatb.2022.121953.

References

[1] E.E. Benson, C.P. Kubiak, A.J. Sathrum, J.M. Smieja, Electrocatalytic and homogeneous approaches to conversion of CO_2 to liquid fuels, Chem. Soc. Rev. 38 (2009) 89–99.

[2] Z. Chen, M.-R. Gao, N. Duan, J. Zhang, Y.-Q. Zhang, T. Fan, J. Zhang, Y. Dong, J. Li, Q. Liu, X. Yi, J.-L. Luo, Tuning adsorption strength of CO_2 and its intermediates on tin oxide-based electrocatalyst for efficient CO_2 reduction towards carbonaceous products, Appl. Catal. B: Environ. 277 (2020), 119252.

[3] Z.-L. Wang, C. Li, Y. Yamauchi, Nanostructured nonprecious metal catalysts for electrochemical reduction of carbon dioxide, Nano Today 11 (2016) 373–391.

[4] C. Costentin, M. Robert, J.M. Saveant, Catalysis of the electrochemical reduction of carbon dioxide, Chem. Soc. Rev. 42 (2013) 2423–2436.

[5] X. Duan, J. Xu, Z. Wei, J. Ma, S. Guo, S. Wang, H. Liu, S. Dou, Metal-free carbon materials for CO_2 electrochemical reduction, Adv. Mater. 29 (2017), 1701784.

[6] L. Zhang, Z.-J. Zhao, J. Gong, Nanostructured materials for heterogeneous electrocatalytic CO_2 reduction and their related reaction mechanisms, Angew. Chem. Int. Ed. 56 (2017) 11326–11353.

[7] T. Wang, Q. Zhao, Y. Fu, C. Lei, B. Yang, Z. Li, L. Lei, G. Wu, Y. Hou, Carbon-rich nonprecious metal single atom electrocatalysts for CO_2 reduction and hydrogen evolution, Small Methods 3 (2019), 1900210.

[8] Y. Cheng, S. Zhao, B. Johannessen, J.P. Veder, M. Saunders, M.R. Rowles, M. Cheng, C. Liu, M.F. Chisholm, R. De Marco, H.M. Cheng, S.Z. Yang, S.P. Jiang, Atomically dispersed transition metals on carbon nanotubes with ultrahigh loading for selective electrochemical carbon dioxide reduction, Adv. Mater. 30 (2018), 1706287.

[9] F. Pan, W. Deng, C. Justiniano, Y. Li, Identification of champion transition metals centers in metal and nitrogen-codoped carbon catalysts for CO_2 reduction, Appl. Catal. B: Environ. 226 (2018) 463–472.

[10] S.-G. Han, D.-D. Ma, S.-H. Zhou, K. Zhang, W.-B. Wei, Y. Du, X.-T. Wu, Q. Xu, R. Zou, Q.-L. Zhu, Fluorine-tuned single-atom catalysts with dense surface Ni-N_4 sites on ultrathin carbon nanosheets for efficient CO_2 electroreduction, Appl. Catal. B: Environ. 283 (2021), 119591.

[11] C.M. Ding, C.C. Feng, Y.H. Mei, F.Y. Liu, H. Wang, M. Dupuis, C. Li, Carbon nitride embedded with transition metals for selective electrocatalytic CO_2 reduction, Appl. Catal. B: Environ. 268 (2020), 118391.

[12] A.S. Varela, N. Ranjbar Sahraie, J. Steinberg, W. Ju, H.S. Oh, P. Strasser, Metal-doped nitrogenated carbon as an efficient catalyst for direct CO_2 electroreduction to CO and hydrocarbons, Angew. Chem. Int. Ed. 54 (2015) 10758–10762.

[13] W. Zheng, J. Yang, H. Chen, Y. Hou, Q. Wang, M. Gu, F. He, Y. Xia, Z. Xia, Z. Li, B. Yang, L. Lei, C. Yuan, Q. He, M. Qiu, X. Feng, Atomically defined

undercoordinated active sites for highly efficient CO_2 electroreduction, Adv. Funct. Mater. 30 (2019), 1907658.

[14] M. Feng, X. Wu, H. Cheng, Z. Fan, X. Li, F. Cui, S. Fan, Y. Dai, G. Lei, G. He, Well-defined Fe–Cu diatomic sites for efficient catalysis of CO_2 electroreduction, J. Mater. Chem. A 9 (2021) 23817–23827.

[15] W. Zhu, L. Zhang, S. Liu, A. Li, X. Yuan, C. Hu, G. Zhang, W. Deng, K. Zang, J. Luo, Y. Zhu, M. Gu, Z.-J. Zhao, J. Gong, Enhanced CO_2 electroreduction on neighboring Zn/Co monomers by electronic effect, Angew. Chem. Int. Ed. 59 (2020) 12664–12668.

[16] W. Ren, X. Tan, W. Yang, C. Jia, S. Xu, K. Wang, S.C. Smith, C. Zhao, Isolated diatomic Ni-Fe metal–nitrogen sites for synergistic electroreduction of CO_2, Angew. Chem. Int. Ed. 58 (2019) 6972–6976.

[17] R. Li, D. Wang, Superiority of dual-atom catalysts in electrocatalysis: one step further than single-atom catalysts, Adv. Energy Mater. 12 (2022), 2103564.

[18] Y. Pan, C. Zhang, Z. Liu, C. Chen, Y. Li, Structural regulation with atomic-level precision: from single-atomic site to diatomic and atomic interface catalysis, Matter 2 (2020) 78–110.

[19] G. Luo, Y. Jing, Y. Li, Rational design of dual-metal-site catalysts for electroreduction of carbon dioxide, J. Mater. Chem. A 8 (2020) 15809–15815.

[20] W. Cheng, X.F. Lu, D. Luan, X.W. Lou, NiMn-based bimetal-organic framework nanosheets supported on multi-channel carbon fibers for efficient oxygen electrocatalysis, Angew. Chem. Int. Ed. 59 (2020) 18234–18239.

[21] G. Kresse, J. Hafner, Ab initio molecular dynamics for liquid metals, Phys. Rev. B 47 (1993) 558.

[22] G. Kresse, J. Furthmüller, Efficient iterative schemes for ab initio total-energy calculations using a plane-wave basis set, Phys. Rev. B 54 (1996) 11169.

[23] G. Kresse, J. Furthmüller, Efficiency of ab-initio total energy calculations for metals and semiconductors using a plane-wave basis set, Comput. Mater. Sci. 6 (1996) 15–50.

[24] J.P. Perdew, K. Burke, M. Ernzerhof, Generalized gradient approximation made simple, Phys. Rev. Lett. 77 (1996) 3865.

[25] P.E. Blöchl, Projector augmented-wave method, Phys. Rev. B 50 (1994) 17953.

[26] S. Grimme, Semiempirical GGA-type density functional constructed with a long-range dispersion correction, J. Comput. Chem. 27 (2006) 1787.

[27] H.J. Monkhorst, J.D. Pack, Special points for Brillouin-zone integrations, Phys. Rev. B 13 (1976) 5188.

[28] Z.-Q. Zhao, X. Chen, Q. Yang, J.-H. Liu, X.-J. Huang, Selective adsorption toward toxic metal ions results in selective response: electrochemical studies on a polypyrrole/reduced graphene oxide nanocomposite, Chem. Commun. 48 (2012) 2180–2182.

[29] H. Han, Y. Noh, Y. Kim, V.S.K. Yadav, S. Park, W. Yoon, S. Lee, W.B. Kim, Electrocatalytic oxidations of formic acid and ethanol over Pd catalysts supported on a doped polypyrrole-carbon composite, ChemistrySelect 2 (2017) 6260–6268.

[30] H. Han, Y. Noh, Y. Kim, S. Park, W. Yoon, D. Jang, S.M. Choi, W.B. Kim, Selective electrochemical CO_2 conversion to multicarbon alcohols on highly efficient N-doped porous carbon-supported Cu catalysts, Green Chem. 22 (2020) 71–84.

[31] H. Han, S. Jin, S. Park, M.H. Seo, W.B. Kim, Atomic iridium species anchored on porous carbon network support: an outstanding electrocatalyst for CO_2 conversion to CO, Appl. Catal. B: Environ. 292 (2021), 120173.

[32] Y. Zhao, J. Liang, C. Wang, J. Ma, G.G. Wallace, Tunable and efficient tin modified nitrogen-doped carbon nanofibers for electrochemical reduction of aqueous carbon dioxide, Adv. Energy Mater. 8 (2018), 1702524.

[33] H. Han, Y. Noh, Y. Kim, W.S. Jung, S. Park, W.B. Kim, An N-doped porous carbon network with a multidirectional structure as a highly efficient metal-free catalyst for the oxygen reduction reaction, Nanoscale 11 (2019) 2423–2433.

[34] T. Zheng, K. Jiang, N. Ta, Y. Hu, J. Zeng, J. Liu, H. Wang, Large-scale and highly selective CO_2 electrocatalytic reduction on nickel single-atom catalyst, Joule 3 (2019) 265–278.

[35] L. Bai, Z. Duan, X. Wen, R. Si, J. Guan, Atomically dispersed manganese-based catalysts for efficient catalysis of oxygen reduction reaction, Appl. Catal. B: Environ. 257 (2019), 117930.

[36] J. Li, W.-Y. Zan, H. Kang, Z. Dong, X. Zhang, Y. Lin, Y.-W. Mu, F. Zhang, X.-M. Zhang, J. Gu, Graphitic-N highly doped graphene-like carbon: a superior metal-free catalyst for efficient reduction of CO_2, Appl. Catal. B: Environ. 298 (2021), 120510.

[37] H. Xu, D. Cheng, D. Cao, X.C. Zeng, A universal principle for a rational design of single-atom electrocatalysts, Nat. Catal. 1 (2018) 339–348.

[38] H.B. Yang, S.-F. Hung, S. Liu, K. Yuan, S. Miao, L. Zhang, X. Huang, H.-Y. Wang, W. Cai, R. Chen, J. Gao, X. Yang, W. Chen, Y. Huang, H.M. Chen, C.M. Li, T. Zhang,

B. Liu, Atomically dispersed Ni(I) as the active site for electrochemical CO_2 reduction, Nat. Energy 3 (2018) 140–147.

[39] A. Kumar, V.Q. Bui, J. Lee, L. Wang, A.R. Jadhav, X. Liu, X. Shao, Y. Liu, J. Yu, Y. Hwang, H.T.D. Bui, S. Ajmal, M.G. Kim, S.-G. Kim, G.-S. Park, Y. Kawazoe, H. Lee, Moving beyond bimetallic-alloy to single-atom dimer atomic-interface for all-pH hydrogen evolution, Nat. Commun. 12 (2021) 6766.

[40] B. Zhang, J. Zhang, J. Shi, D. Tan, L. Liu, F. Zhang, C. Lu, Z. Su, X. Tan, X. Cheng, B. Han, L. Zheng, J. Zhang, Manganese acting as a high-performance heterogeneous electrocatalyst in carbon dioxide reduction, Nat. Commun. 10 (2019) 2980.

[41] R.I. Masel, Z. Liu, H. Yang, J.J. Kaczur, D. Carrillo, S. Ren, D. Salvatore, C. P. Berlinguette, An industrial perspective on catalysts for low-temperature CO_2 electrolysis, Nat. Nanotechnol. 16 (2021) 118–128.

[42] S. Jin, Z. Hao, K. Zhang, Z. Yan, J. Chen, Advances and challenges for the electrochemical reduction of CO_2 to CO: from fundamentals to industrialization, Angew. Chem. Int. Ed. 60 (2021) 20627–20648.

[43] T. Möller, W. Ju, A. Bagger, X. Wang, F. Luo, T.N. Thanh, A.S. Varela, J. Rossmeisl, P. Strasser, Efficient CO_2 to CO electrolysis on solid Ni–N–C catalysts at industrial current densities, Energy Environ. Sci. 12 (2019) 640–647.

[44] C. Oloman, H. Li, Electrochemical processing of carbon dioxide, ChemSusChem 1 (2008) 385–391.

[45] X. Li, P. Anderson, H.-R.M. Jhong, M. Paster, J.F. Stubbins, P.J.A. Kenis, Greenhouse gas emissions, energy efficiency, and cost of synthetic fuel production using electrochemical CO_2 conversion and the Fischer–Tropsch process, Energy Fuels 30 (2016) 5980–5989.

[46] H. Han, S. Park, D. Jang, S. Lee, W.B. Kim, Electrochemical reduction of CO_2 to CO by N,S dual-doped carbon nanoweb catalysts, ChemSusChem 13 (2020) 539–547.

[47] S. Gao, Y. Lin, X. Jiao, Y. Sun, Q. Luo, W. Zhang, D. Li, J. Yang, Y. Xie, Partially oxidized atomic cobalt layers for carbon dioxide electroreduction to liquid fuel, Nature 529 (2016) 68–71.

[48] Z. Zhang, X. Kong, Q. Li, J. Ke, J. Zeng, Engineering electronic structures of nanomaterials toward carbon dioxide electroreduction, Curr. Opin. Electrochem. 17 (2019) 7–15.

[49] Y. Zhou, F. Che, M. Liu, C. Zou, Z. Liang, P.D. Luna, H. Yuan, J. Li, Z. Wang, H. Xie, H. Li, P. Chen, E. Bladt, R. Quintero-Bermudez, T.-K. Shan, S. Bals, J. Hofkens, D. Sinton, G. Chen, E.H. Sergent, Dopant-induced electron localization drives CO_2 reduction to C_2 hydrocarbons, Nat. Chem. 10 (2018) 974–980.

[50] M.R. Singh, J.D. Goodpaster, A.Z. Weber, M. Head-Gordon, A.T. Bell, Mechanistic insights into electrochemical reduction of CO_2 over Ag using density functional theory and transport models, Proc. Natl. Acad. Sci. USA 114 (2017) E8812–E8821.

[51] Z. Chen, X. Zhang, W. Liu, M. Jiao, K. Mou, X. Zhang, L. Liu, Amination strategy to boost the CO_2 electroreduction current density of M–N/C single-atom catalysts to the industrial application level, Energy Environ. Sci. 14 (2021) 2349–2356.

[52] H. Han, S. Jin, S. Park, D. Jang, M.H. Seo, W.B. Kim, Plasma-induced oxygen vacancies in amorphous MnOx boost catalytic performance for electrochemical CO_2 reduction, Nano Energy 79 (2021), 105492.

[53] K. Chen, M. Cao, G. Ni, S. Chen, H. Liao, L. Zhu, H. Li, J. Fu, E. Cortés, M. Liu, Nickel polyphthalocyanine with electronic localization at the nickel site for enhanced CO_2 reduction reaction, Appl. Catal. B: Environ. 306 (2022), 121093.

[54] Y. Cheng, S. Zhao, H. Li, S. He, J.-P. Veder, B. Johannessen, J. Xiao, S. Lu, J. Pan, M.F. Chisholm, S.-Z. Yang, C. Liu, J.G. Chen, S.P. Jiang, Unsaturated edge-anchored Ni single atoms on porous microwave exfoliated graphene oxide for electrochemical CO_2, Appl. Catal. B: Environ. 243 (2019) 294–303.

[55] Z. Zeng, L.Y. Gan, H.B. Yang, X. Su, J. Gao, W. Liu, H. Matsumoto, J. Gong, J. Zhang, W. Cai, Z. Zhang, Y. Yan, B. Liu, P. Chen, Orbital coupling of hetero-diatomic nickel-iron site for bifunctional electrocatalysis of CO_2 reduction and oxygen evolution, Nat. Commun. 12 (2021) 4088.

[56] R. Wang, R. Wu, X. Yan, D. Liu, P. Guo, W. Li, H. Pan, Implanting single Zn atoms coupled with metallic Co nanoparticles into porous carbon nanosheets grafted with carbon nanotubes for high-performance lithium-sulfur batteries, Adv. Funct. Mater. 32 (2022), 2200424.

[57] W. Ren, X. Tan, C. Jia, A. Krammer, Q. Sun, J. Qu, S.C. Smith, A. Schueler, X. Hu, C. Zhao, Electronic regulation of nickel single atoms by confined nickel nanoparticles for energy-efficient CO_2 electroreduction, Angew. Chem. Int. Ed. (2022), e202203335.

[58] L. Jiao, J. Zhu, Y. Zhang, W. Yang, S. Zhou, A. Li, C. Xie, X. Zheng, W. Zhou, S.-H. Yu, H.-L. Jiang, Non-bonding interaction of neighboring Fe and Ni single-atom pairs on MOF-derived N-doped carbon for enhanced CO_2 electroreduction, J. Am. Chem. Soc. 143 (2021) 19417–19424.